Improved Stability and Electronic Homogeneity in Perovskite Solar Cells via Nanoengineered Buried Oxide Interlayer

W. Hashini K. Perera, Tony J. Woodgate, Dong Kuk Kim, Rachel C. Kilbride, Mateus G. Masteghin, Christopher T. G. Smith, Steven J. Hinder, Sebastian Wood, K. D. G. Imalka Jayawardena*, S. Ravi P. Silva*

W. Hashini K. Perera, Tony J. Woodgate, Mateus G. Masteghin, Christopher T. G. Smith, K. D. G. Imalka Jayawardena*, S. Ravi P. Silva*
Advanced Technology Institute, School of Computer Science and Electronic Engineering, University of Surrey, Guildford, Surrey GU2 7XH, UK.

Dong Kuk Kim, Sebastian Wood
Electromagnetic and Electrochemical Technologies Division, National Physical Laboratory, Teddington, Middlesex, TW11 0LW UK.

Rachel C. Kilbride
Department of Chemistry, University of Sheffield, Sheffield S3 7HF, UK.

Steven J. Hinder
The Surface Analysis Laboratory, Faculty of Engineering and Physical Sciences, University of Surrey, Guildford, Surrey GU2 7XH, UK.

E-mail: s.silva@surrey.ac.uk, i.jayawardena@surrey.ac.uk

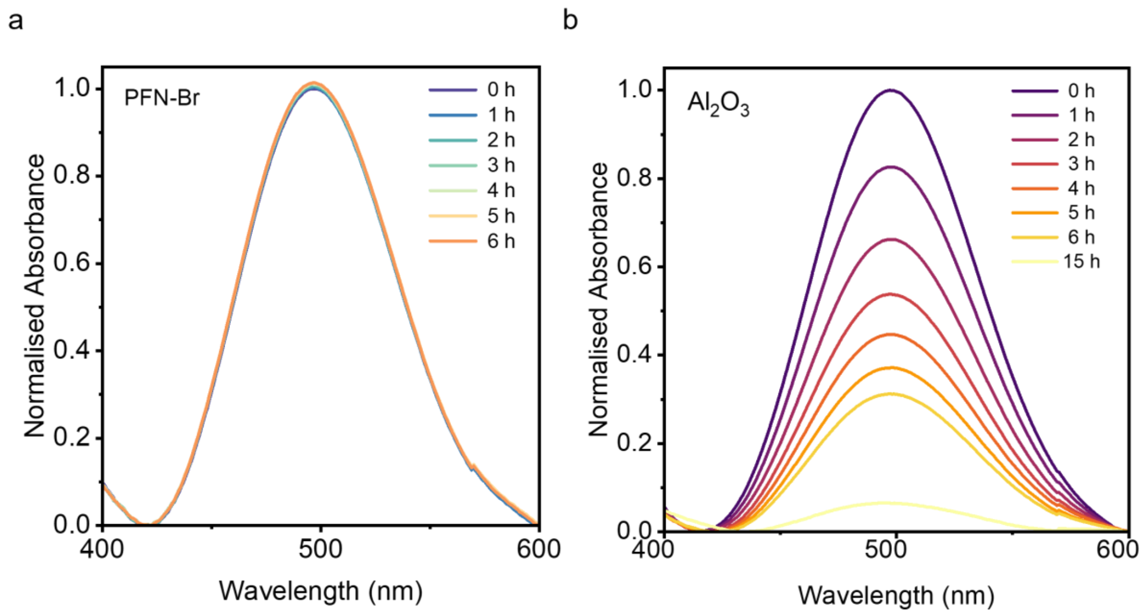

Figure S1. UV-Vis absorbance spectra showing the behavior of I_2 absorbance peak with (a) PFN-Br powder and (b) Al_2O_3 powder.

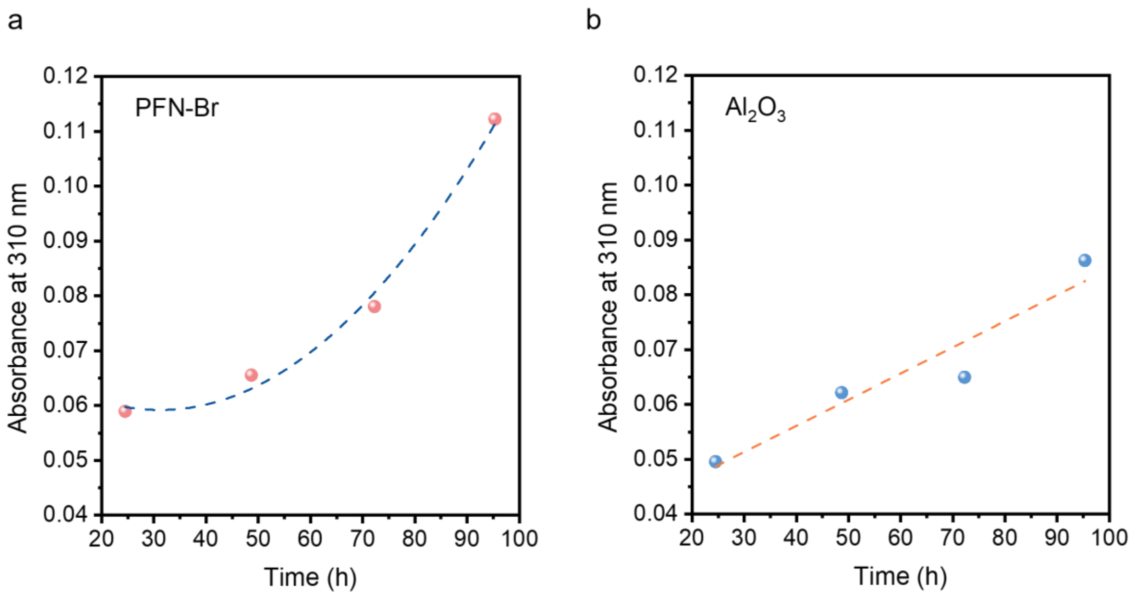

Figure S2. Study of the liberation of iodine from perovskite films formed on (a) Me-4PACz/PFN-Br and (b) Me-4PACz/Al_2O_3 using UV-Vis absorbance spectroscopy. Perovskite films were placed in toluene and heated at 65 °C in the dark.

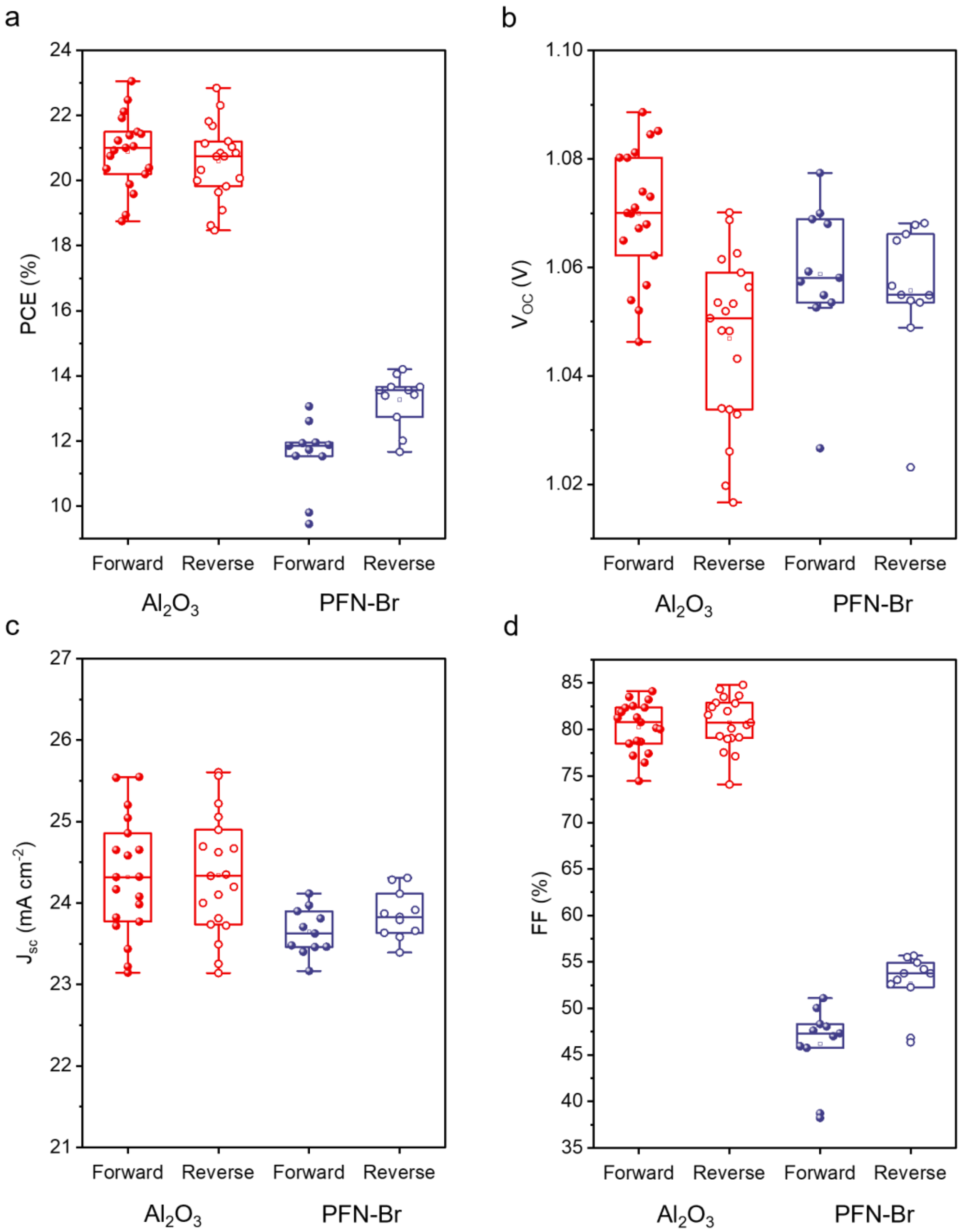

Figure S3. Statistical distribution of device parameters, (a) PCE (b) V_{OC} (c) J_{SC} and (d) FF, for Al_2O_3 and PFN-Br based PSCs with 1.55 eV bandgap.

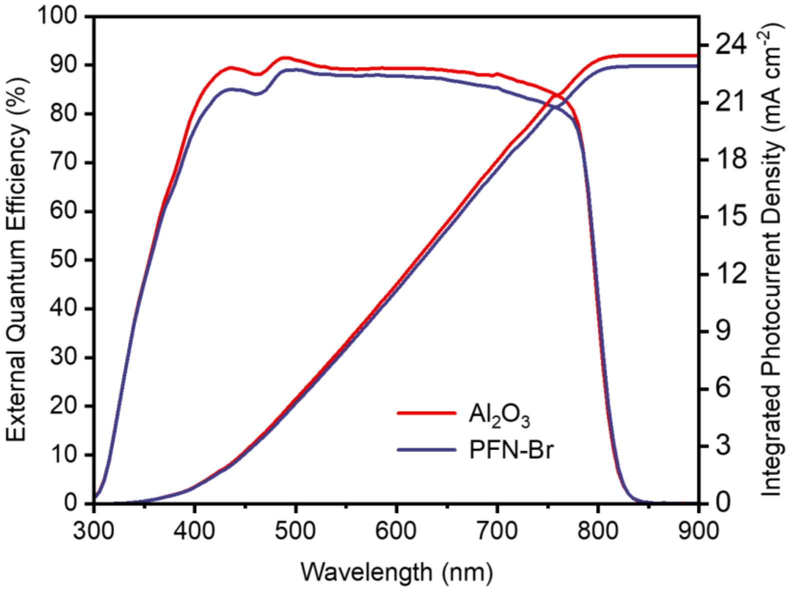

Figure S4. External quantum efficiency (EQE) of the champion devices based on Al_2O_3 and PFN-Br (measured in air) fabricated with 1.55 eV bandgap perovskite. The difference between the J_{SC} obtained from *J-V* data and the integrated photocurrent is due to the degradation of thiocyanate containing perovskites when exposed to moisture.

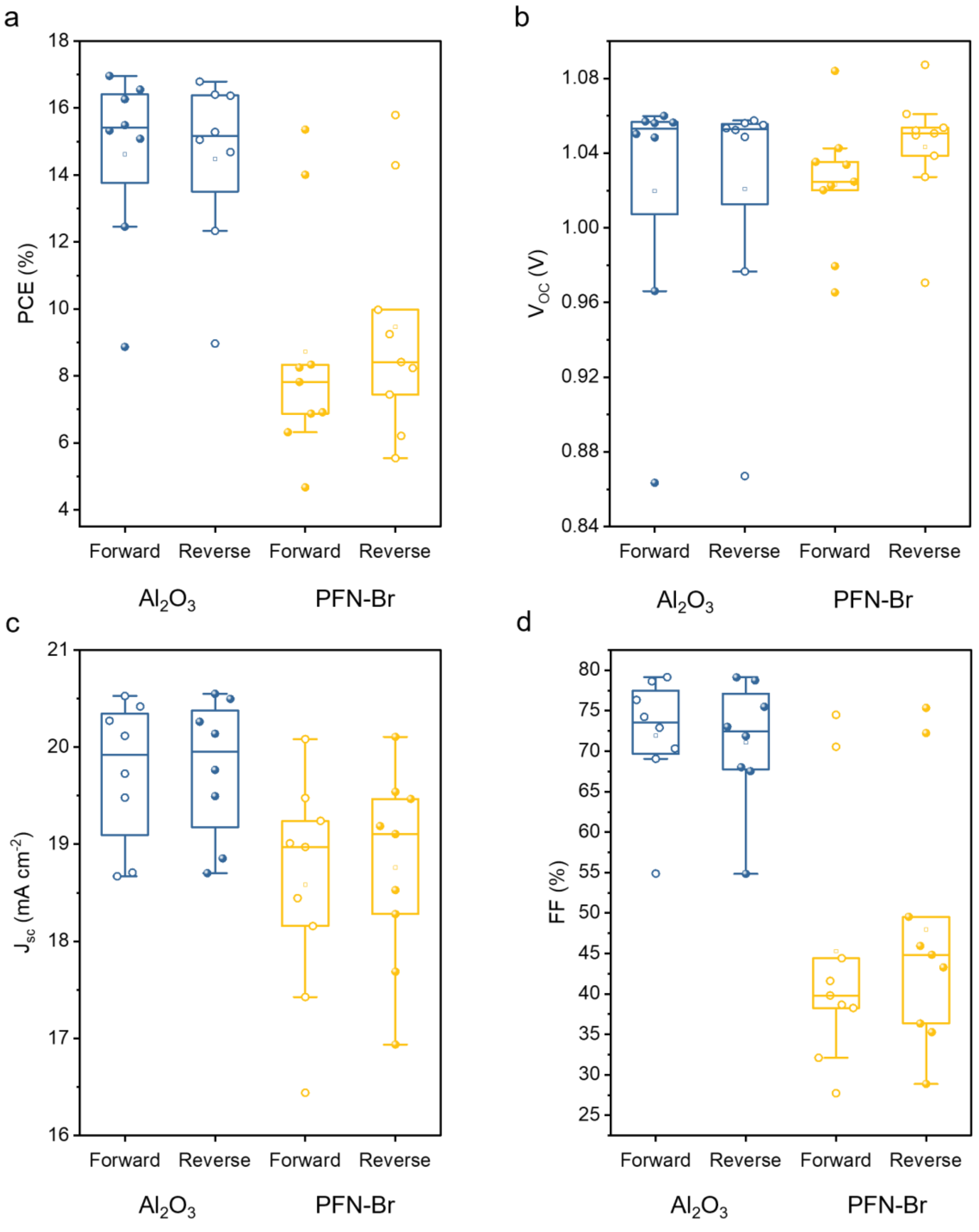

Figure S5. Statistical distribution of device parameters, (a) PCE (b) V_{OC} (c) J_{SC} and (d) FF, for Al_2O_3 and PFN-Br based PSCs with 1.63 eV bandgap used for stability testing.

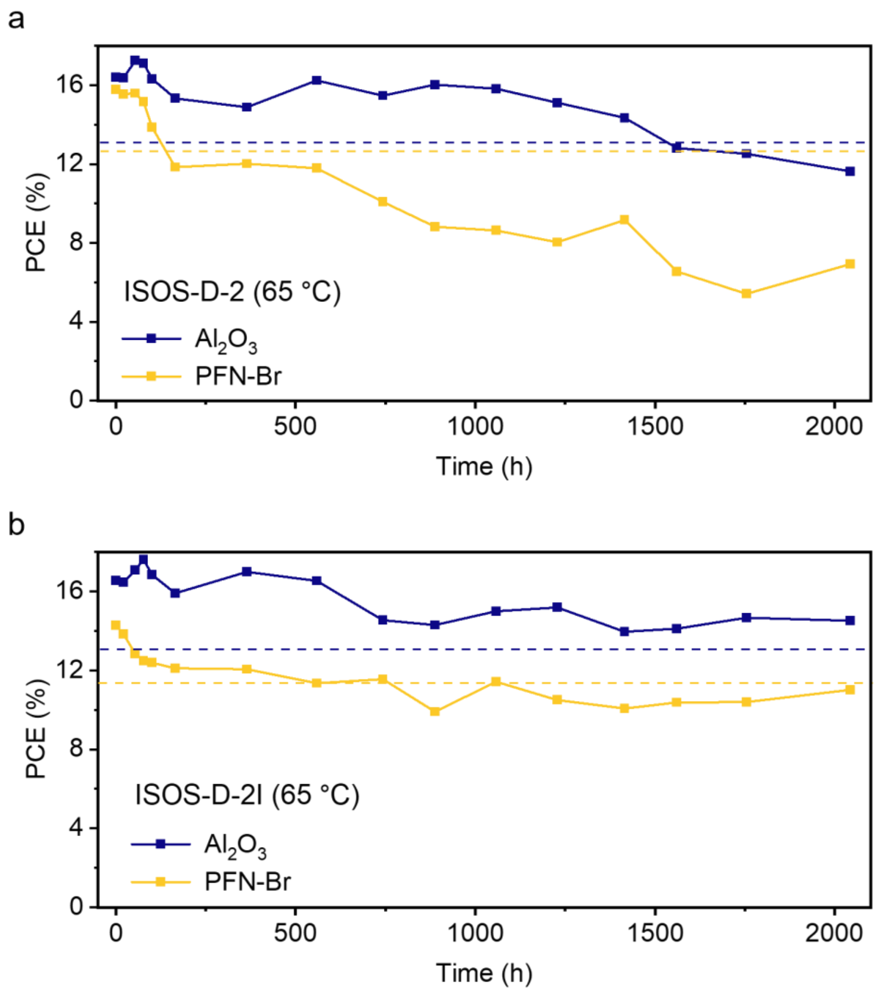

Figure S6. Stability testing of champion PSCs based on PFN-Br and Al_2O_3 NPs under (a) ISOS-D-2, and (b) ISOS-D-2I conditions.

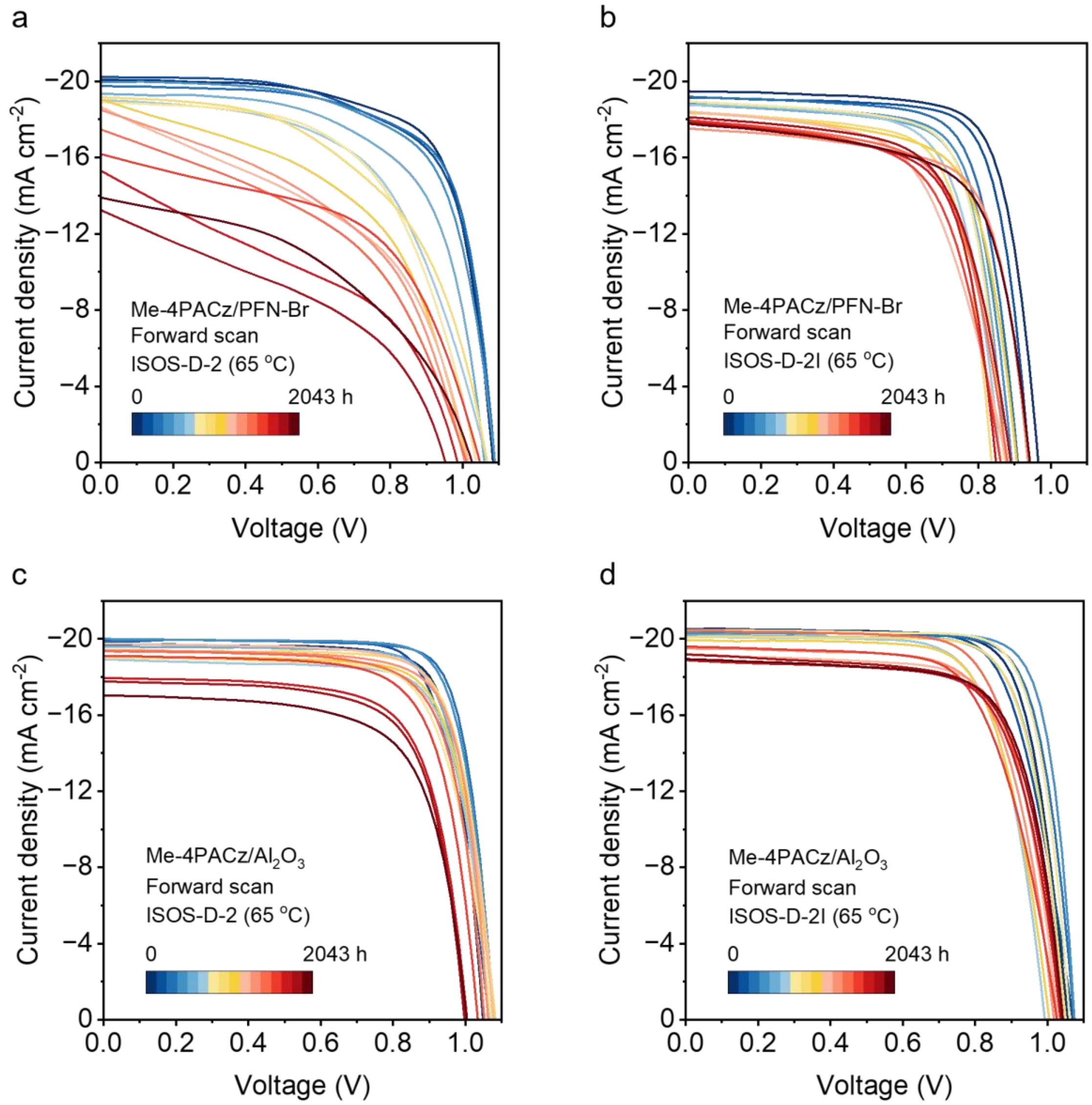

Figure S7. J-V curves in forward scan direction of champion devices based on (a) PFN-Br under ISOS-D-2 conditions, (b) PFN-Br under ISOS-D-2I conditions, (c) Al_2O_3 under ISOS-D-2 conditions, and (d) Al_2O_3 under ISOS-D-2I conditions.

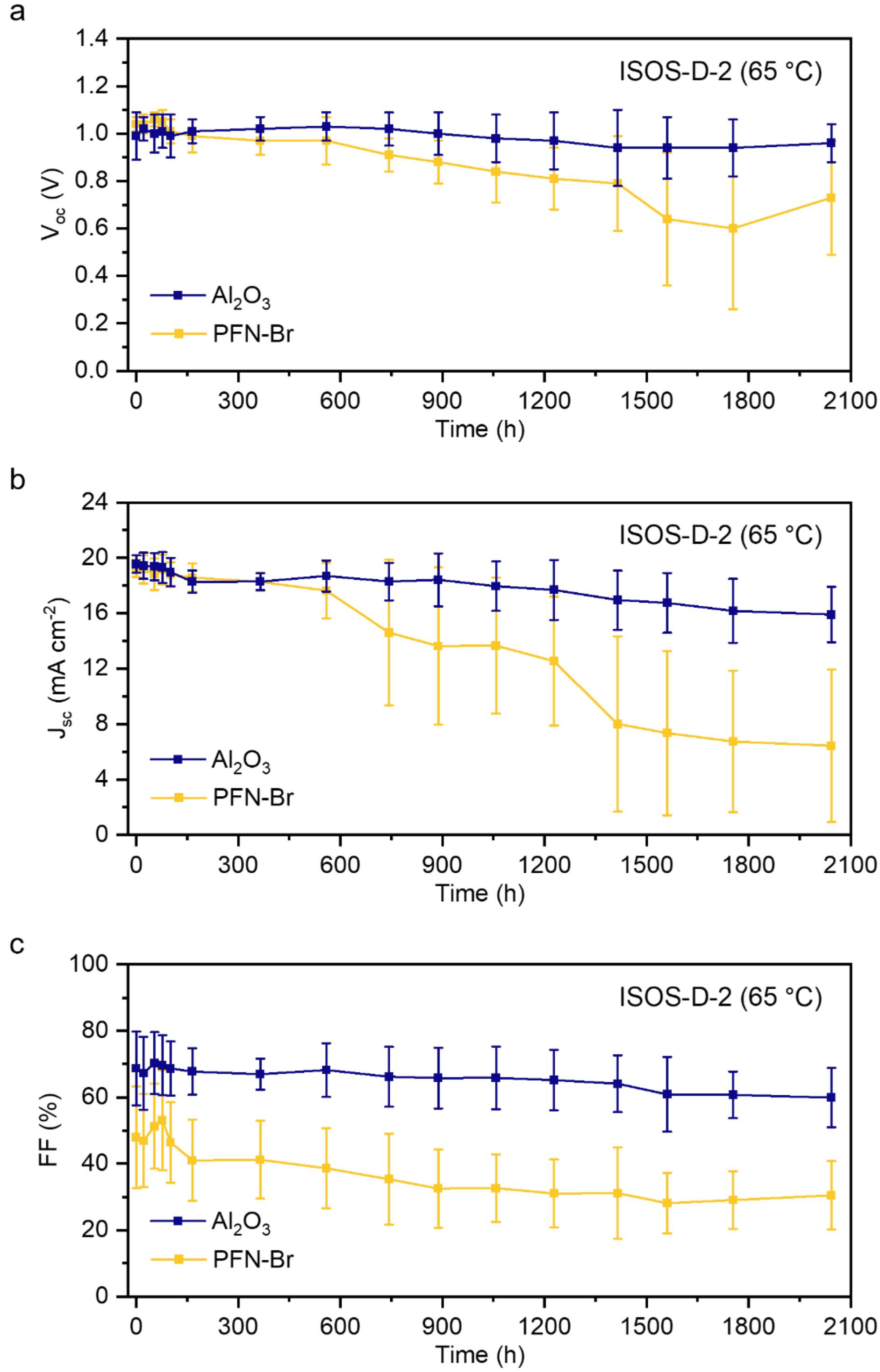

Figure S8. Variation of device parameters, (a) V_{OC} (b) J_{SC} and (c) FF, of PSCs based on Al_2O_3 and PFN-Br under ISOS -D-2 stability testing conditions.

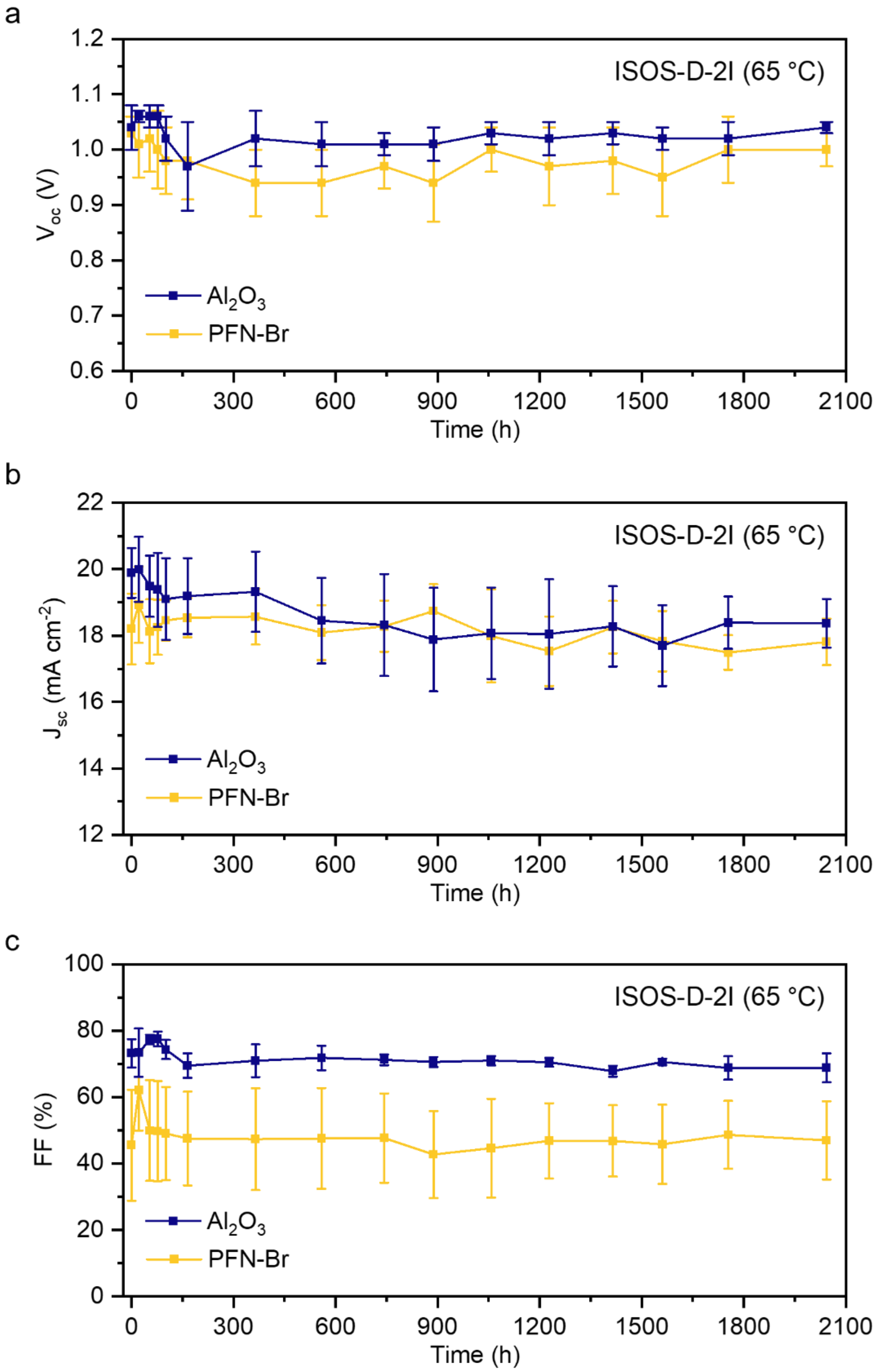

Figure S9. Variation of device parameters, (a) V_{OC} (b) J_{SC} and (c) FF, of PSCs based on Al_2O_3 and PFN-Br under ISOS -D-2I stability testing conditions.

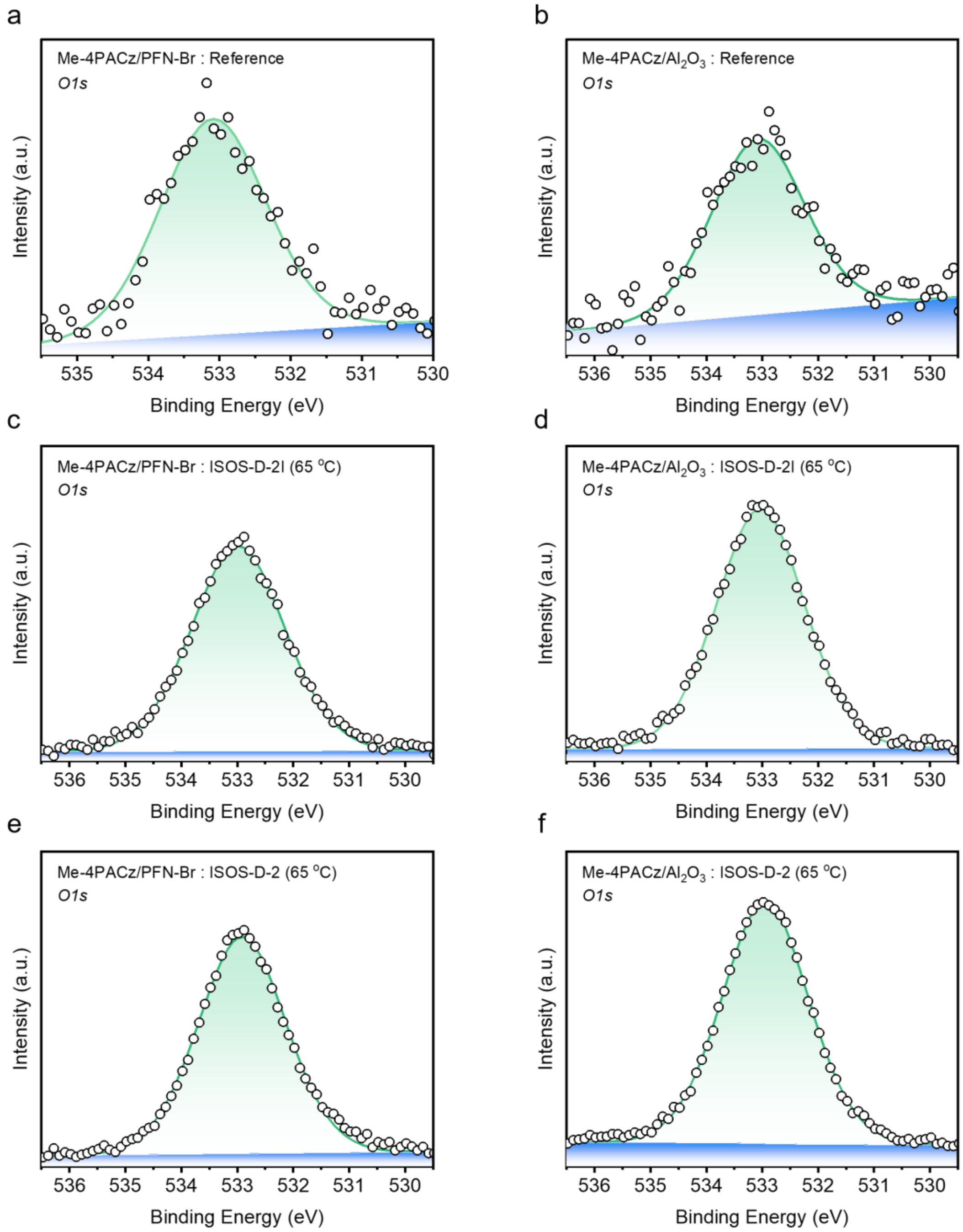

Figure S10. O1s XPS spectra of fresh and degraded perovskite films on Me-4PACz modified with the different surface modifiers. Fresh films on (a) PFN-Br and (b) Al_2O_3. Films degraded under ISOS-D-2I conditions on (c) PFN-Br and (b) Al_2O_3. Films degraded under ISOS-D-2 conditions on (e) PFN-Br and (f) Al_2O_3.

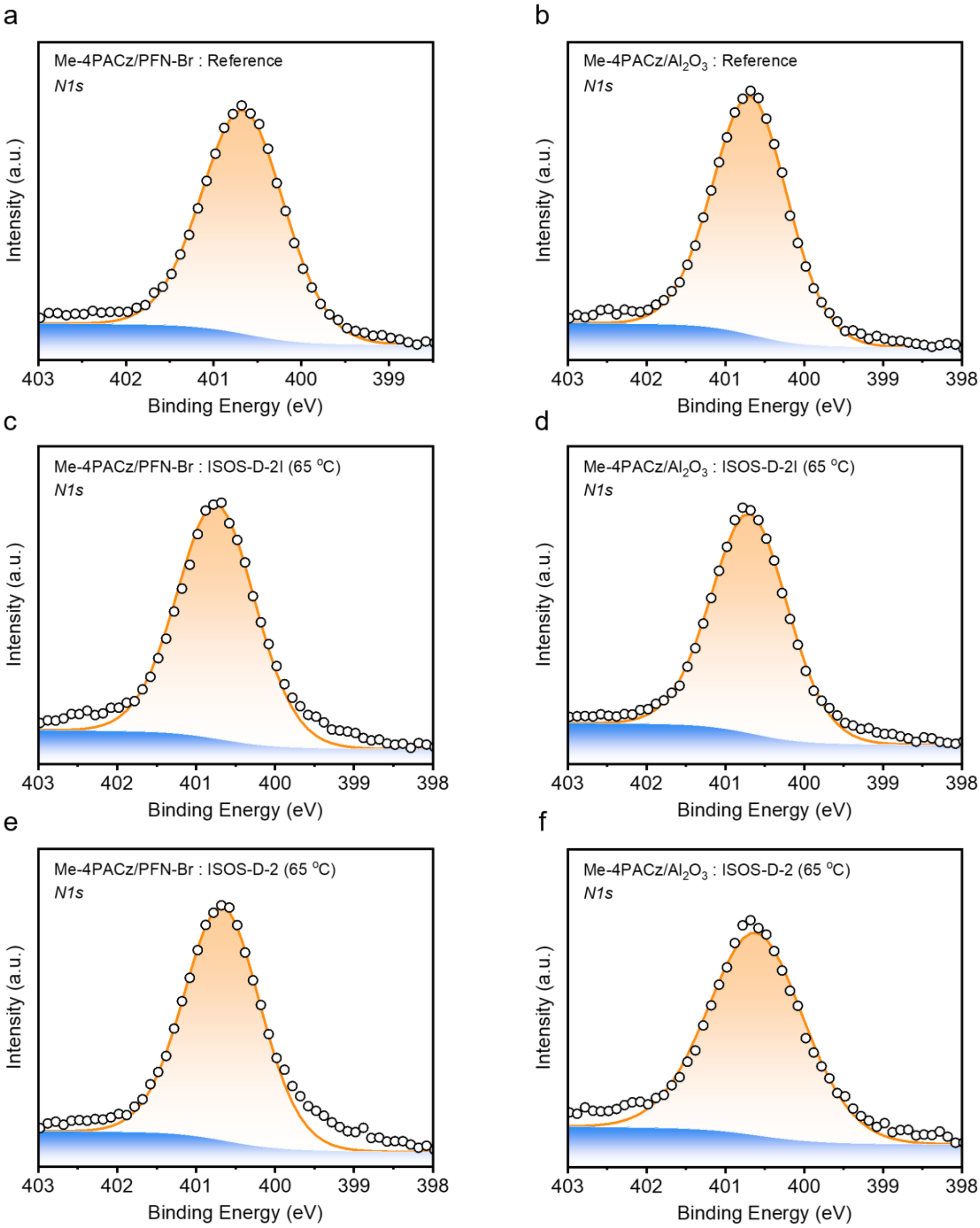

Figure S11. N1s XPS spectra of fresh and degraded perovskite films on Me-4PACz modified with the different surface modifiers. Fresh films on (a) PFN-Br and (b) Al_2O_3. Films degraded under ISOS-D-2I conditions on (c) PFN-Br and (b) Al_2O_3. Films degraded under ISOS-D-2 conditions on (e) PFN-Br and (f) Al_2O_3.

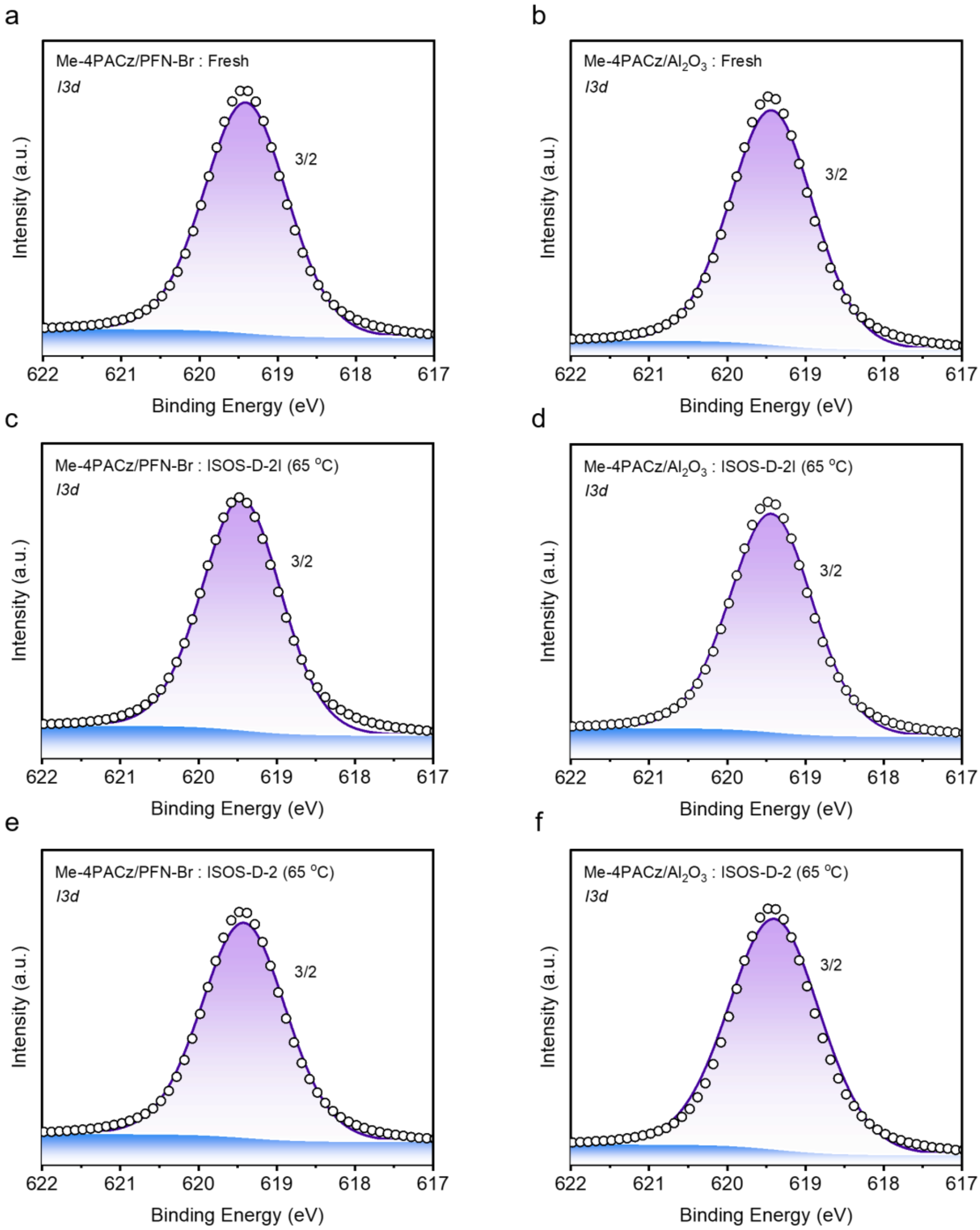

Figure S12. I3d XPS spectra of fresh and degraded perovskite films on Me-4PACz modified with the different surface modifiers. Fresh films on (a) PFN-Br and (b) Al_2O_3. Films degraded under ISOS-D-2I conditions on (c) PFN-Br and (b) Al_2O_3. Films degraded under ISOS-D-2 conditions on (e) PFN-Br and (f) Al_2O_3.

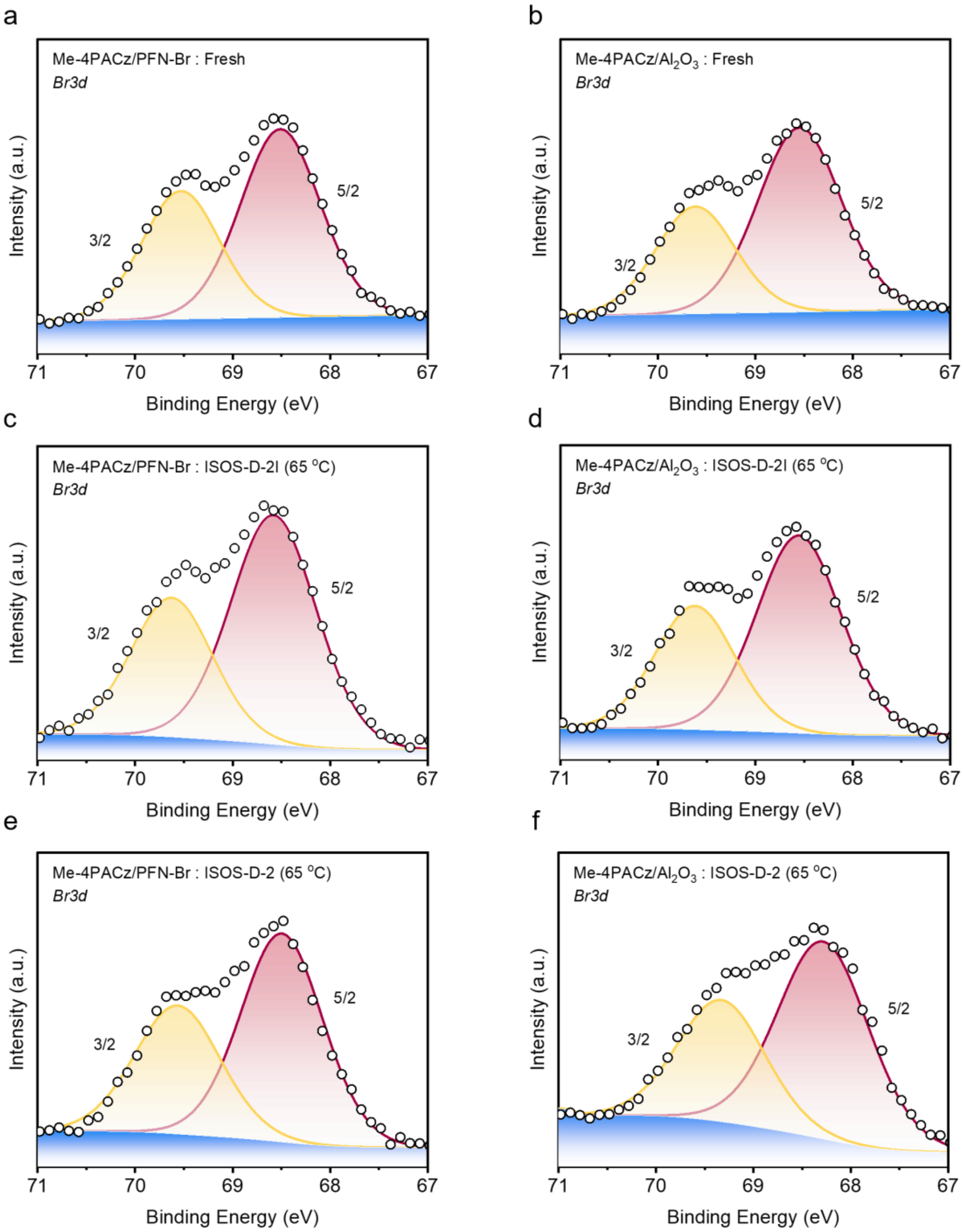

Figure S13. Br3d XPS spectra of fresh and degraded perovskite films on Me-4PACz modified with the different surface modifiers. Fresh films on (a) PFN-Br and (b) Al_2O_3. Films degraded under ISOS-D-2I conditions on (c) PFN-Br and (d) Al_2O_3. Films degraded under ISOS-D-2 conditions on (e) PFN-Br and (f) Al_2O_3.

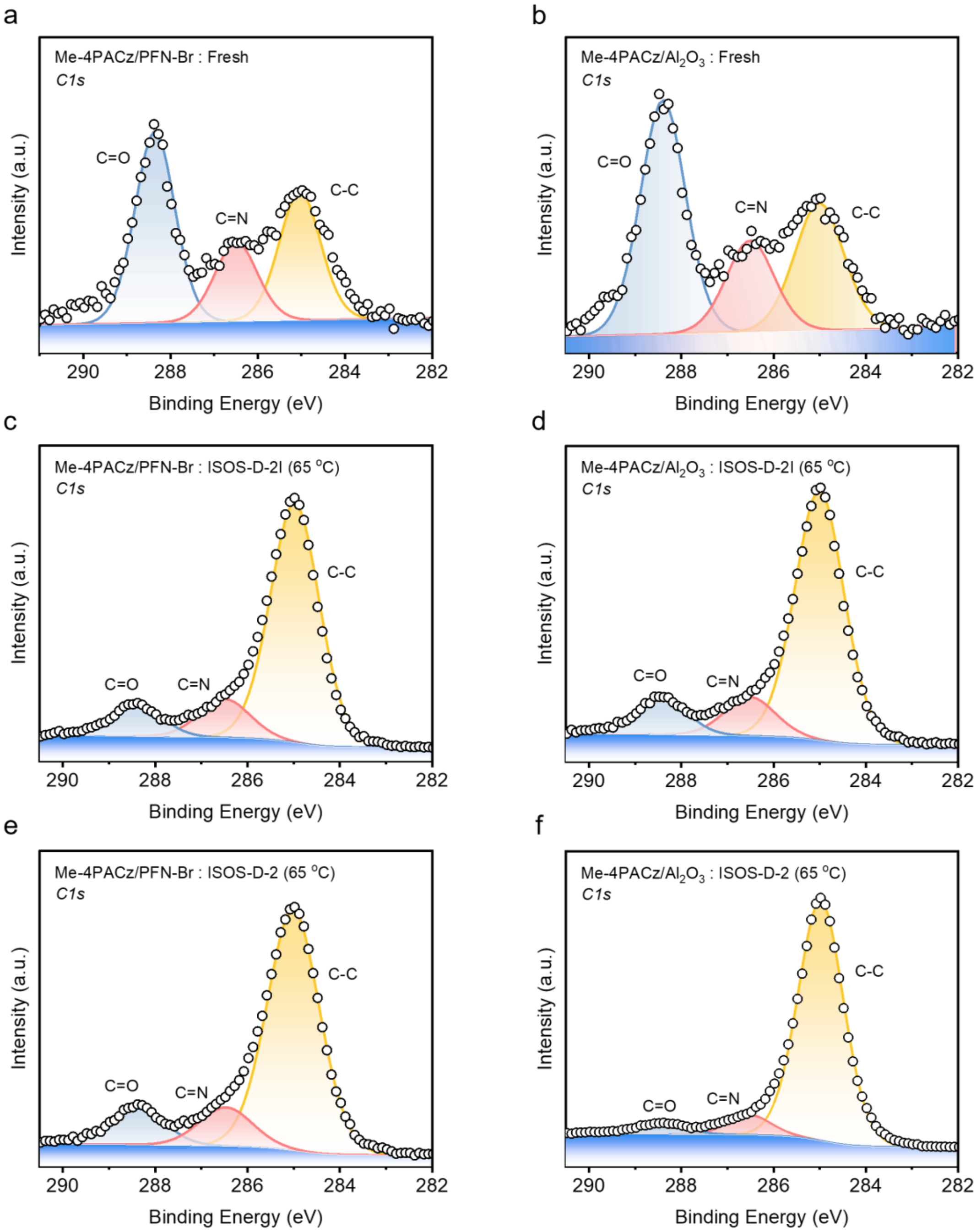

Figure S14. C1s XPS spectra of fresh and degraded perovskite films on Me-4PACz modified with the different surface modifiers. Fresh films on (a) PFN-Br and (b) Al_2O_3. Films degraded under ISOS-D-2I conditions on (c) PFN-Br and (d) Al_2O_3. Films degraded under ISOS-D-2 conditions on (e) PFN-Br and (f) Al_2O_3.

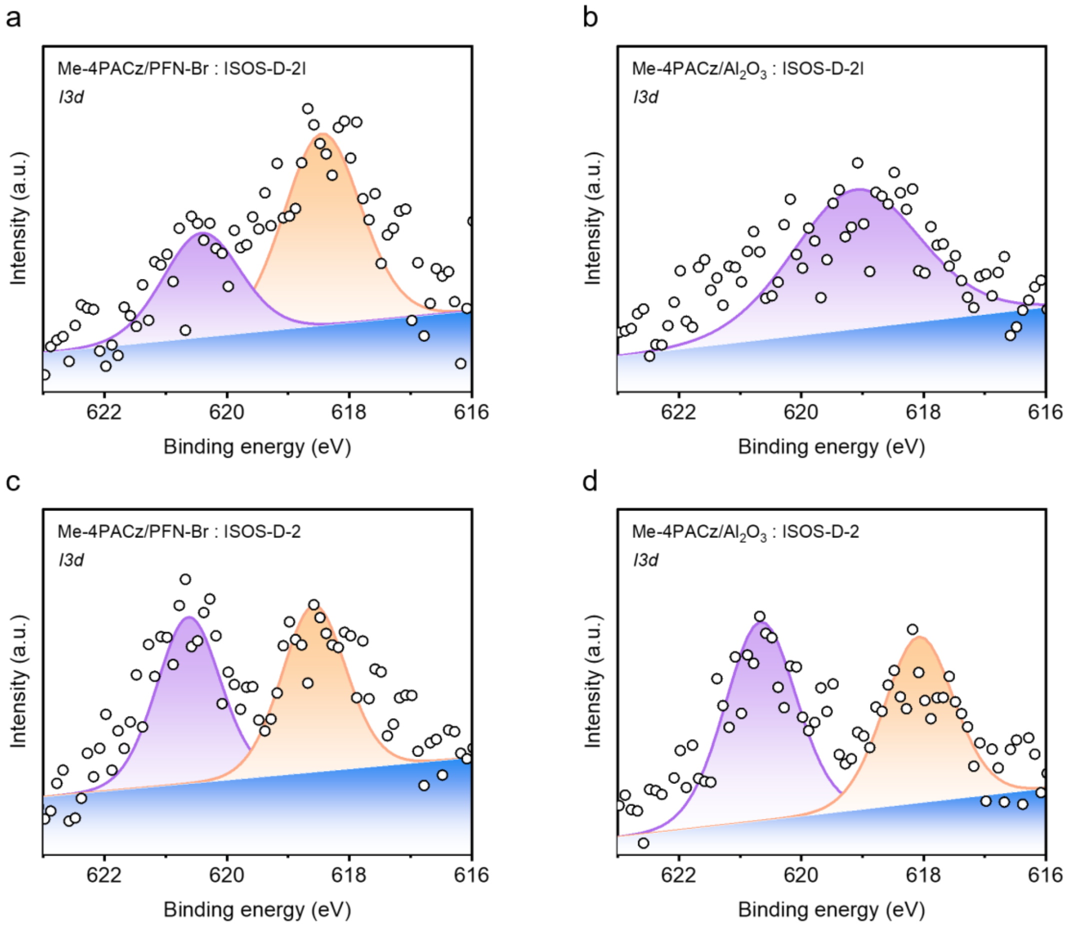

Figure S15. I3d XPS spectra of degraded perovskite films on Me-4PACz modified with the different surface modifiers, with encapsulation. Films degraded under ISOS-D-2I conditions on (a) PFN-Br and (b) Al_2O_3. Films degraded under ISOS-D-2 conditions on (c) PFN-Br and (d) Al_2O_3.

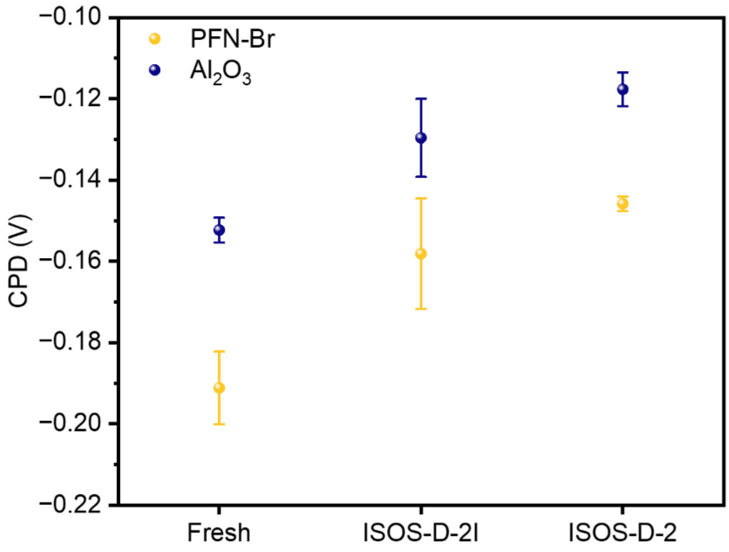

Figure S16. Changes to the mean CPD of perovskites formed on Me-4PACz modified with PFN-Br and Al_2O_3.

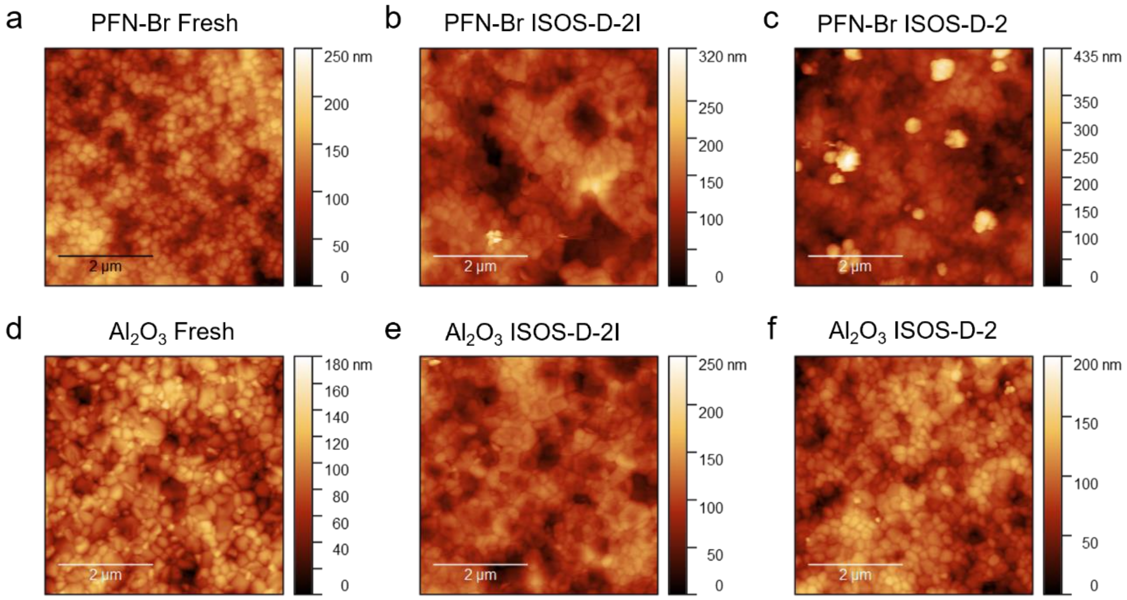

Figure S17. KPFM topography maps of perovskite films. Topography maps of perovskites on PFN-Br: a) Fresh film, (b) degraded film under ISOS-D-2I conditions, and (c) degraded film under ISOS-D-2 conditions. Topography maps of perovskites on Al_2O_3: (d) Fresh film, (e) degraded film under ISOS-D-2I conditions, and (f) degraded film under ISOS-D-2 conditions.

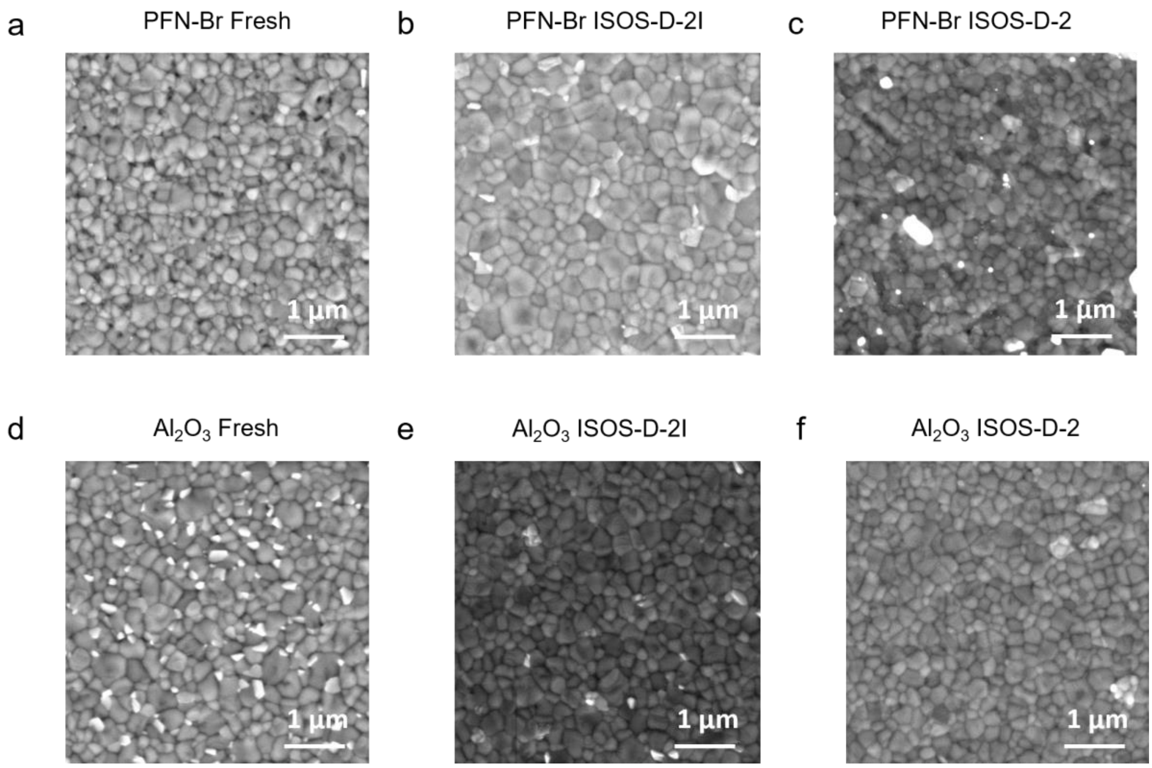

Figure S18. Microstructure of perovskite films. SEM images of perovskites on PFN-Br: a) Fresh film, (b) degraded film under ISOS-D-2I conditions, and (c) degraded film under ISOS-D-2 conditions. SEM images of perovskites on Al_2O_3: (d) Fresh film, (e) degraded film under ISOS-D-2I conditions, and (f) degraded film under ISOS-D-2 conditions.

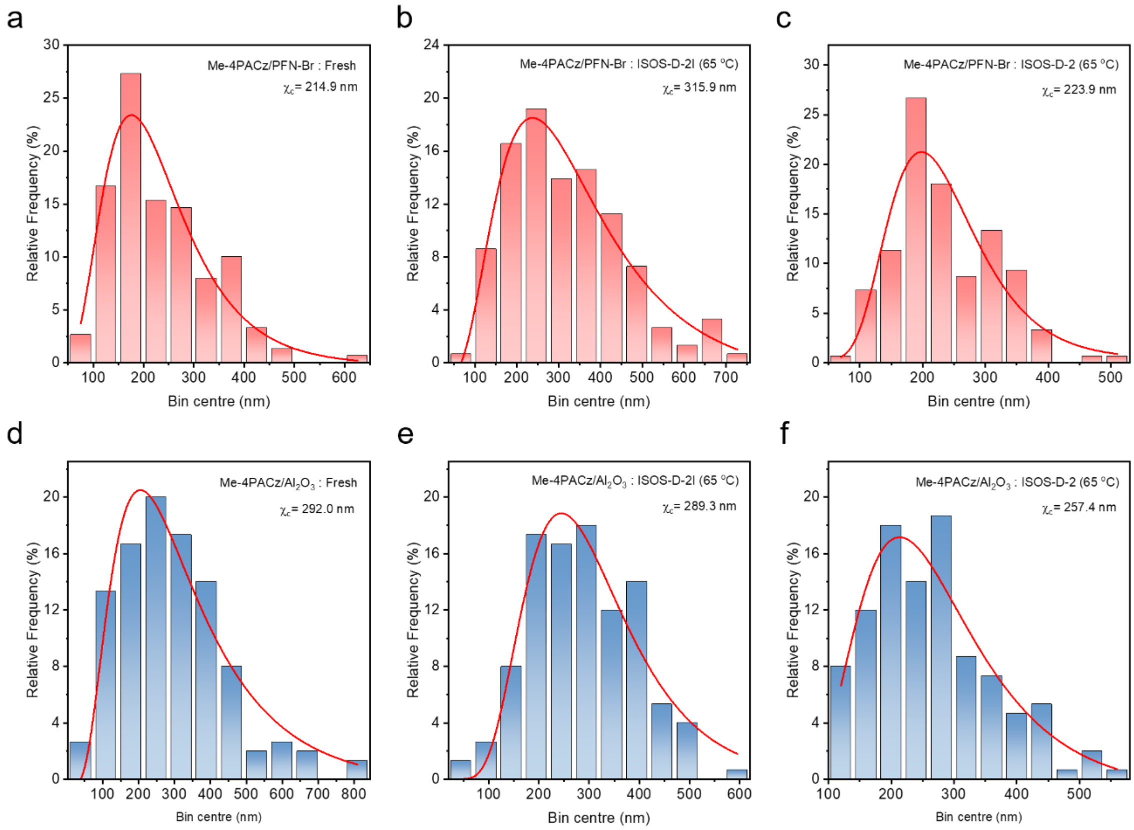

Figure S19. Microstructure of perovskite films. Grain size analysis of perovskites on PFN-Br: a) Fresh film, (b) degraded film under ISOS-D-2I conditions, and (c) degraded film under ISOS-D-2 conditions. Grain size analysis of perovskites on Al_2O_3: (d) Fresh film, (e) degraded film under ISOS-D-2I conditions, and (f) degraded film under ISOS-D-2 conditions.

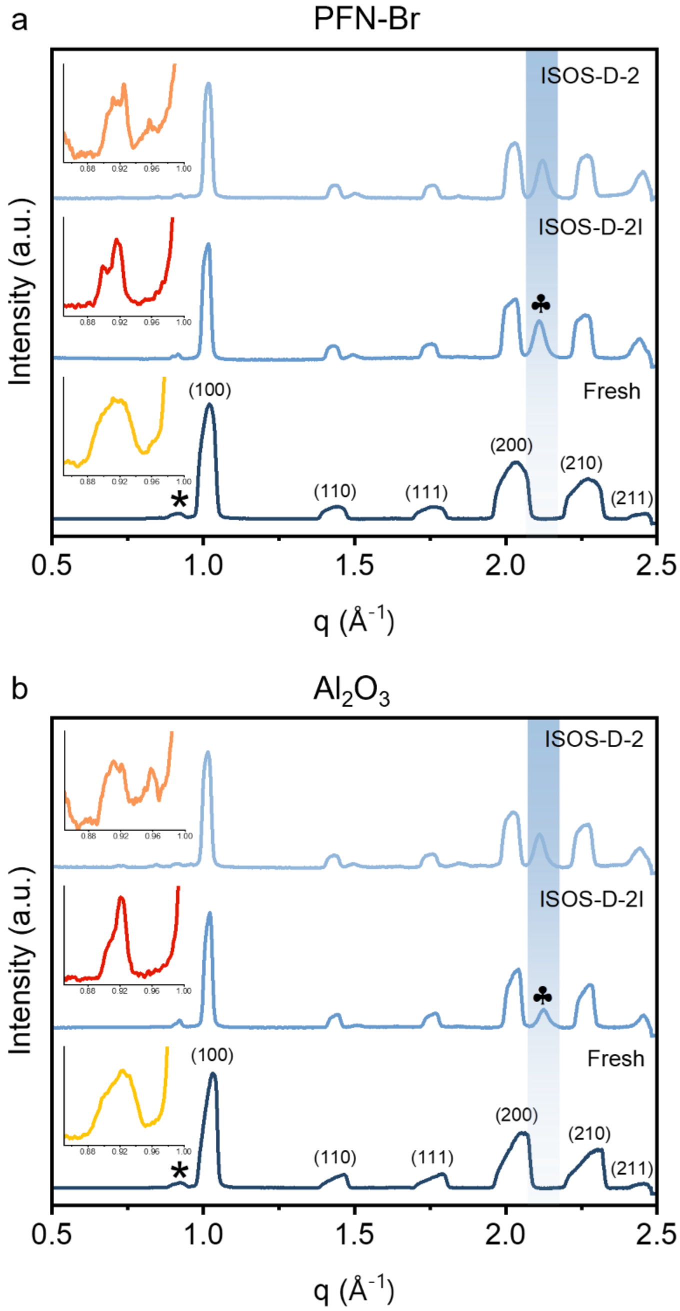

Figure S20. Integrated 1-D peak profiles for perovskite films on Me-4PACz modified with (a) PFN-Br and (b) Al_2O_3. ∗ and ♣ indicate scattering patterns corresponding to PbI_2 and ITO respectively.

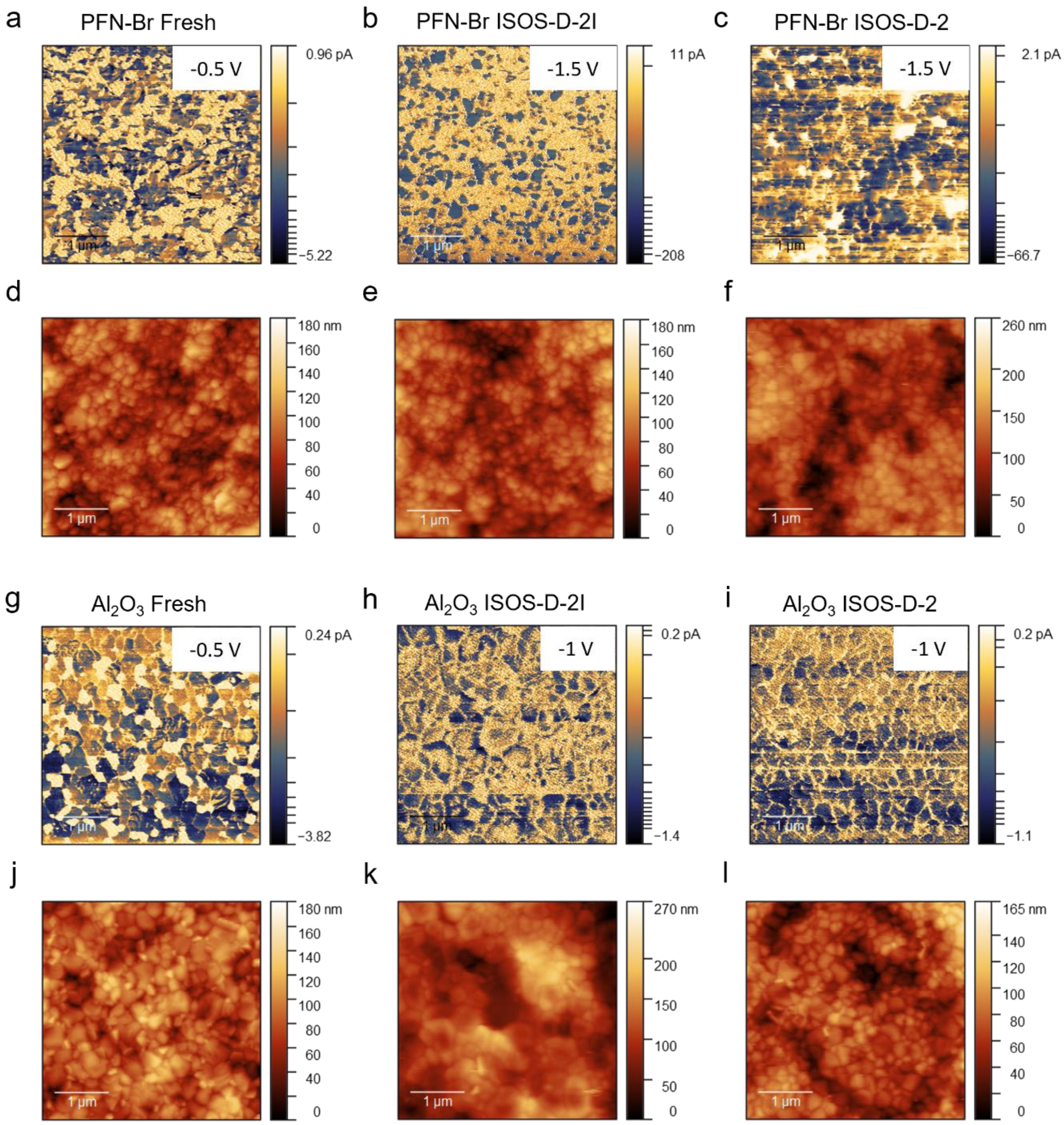

Figure S21. Nanoscale electrical conduction within the perovskite films. (a) – (c) Conducting atomic force microscopy (c-AFM) current mapping of perovskite films on Me-4PACz modified with PFN-Br. (a) Fresh film, (b) Film degraded under ISOS-D-2I conditions, and (c) Film degraded under ISOS-D-2 conditions. (d) – (f) Topography of perovskite films on Me-4PACz modified with PFN-Br. (d) Fresh film, (e) Film degraded under ISOS-D-2I conditions, and (f) Film degraded under ISOS-D-2 conditions. (g) – (i) c-AFM mapping of perovskite films on Me-4PACz modified with Al_2O_3. (g) Fresh film, (h) Film degraded under ISOS-D-2I conditions, and (i) Film degraded under ISOS-D-2 conditions. (j) – (l) c-AFM topography of perovskite films on Me-4PACz modified with Al_2O_3. (j) Fresh film, (k) Film degraded under ISOS-D-2I conditions, and (l) Film degraded under ISOS-D-2 conditions. The topographic AFM scans were obtained at the same locations over which c-AFM maps were obtained for both sample times.